Impact of doping on InAs/GaAs quantum-dot solar cells: A numerical study on photovoltaic and photoluminescence behavior

(Article begins on next page)
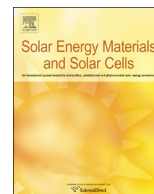
Impact of doping on InAs/GaAs quantum-dot solar cells: A numerical study on photovoltaic and photoluminescence behavior

F. Cappelluti *, M. Gioannini, A. Khalili

Department of Electronics and Telecommunications, Politecnico di Torino, Corso Duca degli Abruzzi 24, 10129 Torino, Italy

ABSTRACT

We investigate the effect of doping on quantum dot (QD) solar cells by analysing their behavior in terms of photovoltaic characteristic, external quantum efficiency, and photoluminescence (PL) at room temperature. The analysis addresses the two most widespread methods for QD selective doping, namely modulation and direct doping, to gain a comprehensive device-level assessment of the impact of doping profile and density on the solar cell behavior. Devices are simulated using a physics-based model that accurately describes QD carrier dynamics within a semi-classical drift-diffusion-Poisson model. Different scenarios in terms of crystal quality are considered: in the high-quality material, close to radiative limit, large open circuit voltage recovery is predicted, due to the suppression of radiative recombination through QD ground state. In the defective material, significant photovoltage recovery is also attained owing to the suppression of both nonradiative and QD ground state radiative recombination. In both cases, PL emission from extended wetting layer states becomes dominant at high doping density. The interplay between nonradiative and QD radiative recombination channels, and how their interaction is modified by doping, are analyzed in detail. Strong influence on the cell behavior of unintentional background doping of interdot layers and markedly nonlinear behavior of open circuit PL with respect to excitation intensity are demonstrated. The resulting picture provides new insight on the experimental results in literature.

© 2016 The Authors. Published by Elsevier B.V. This is an open access article under the CC BY-NC-ND license (http://creativecommons.org/licenses/by-nc-nd/4.0/).

1. Introduction

Self-assembled InAs/GaAs quantum dot solar cells (QDSC) have been investigated since several years for the practical implementation, in the GaAs material system, of the intermediate band (IB) concept [1]. Despite significant technological progresses and experimental demonstration of the basic IB operating principles by QDSCs [2,3], reported devices have not yet met the expectations in terms of enhanced conversion efficiency. The cause is twofold: a weak increase of the short circuit current (J_{sc}) coupled and a large reduction of the open circuit voltage (V_{oc}) with respect to bulk cells. The small enhancement of J_{sc} is inherently related to the small interband optical absorption cross-section per QD layer, which could be circumvented by further optimization of the QD growth, aimed at maximizing the number of stacked QD layers and the QD density, and by photon management via light trapping techniques to enhance the QD effective absorption [4,5]. On the other hand, V_{oc} preservation appears as an even more complex issue. Even though, under 1 sun illumination, some amount of

voltage loss with respect to the reference bulk cell is also predicted by the IB theory, reported V_{oc} penalties are generally much higher than expected. The reason is in the competition between equilibrium and non-equilibrium charge-transfer processes between QD and barrier states [1,6], capture and radiative recombination through QDs of carriers photogenerated in the barrier [7,8], and nonradiative recombination due to defects [9].

Selective QD doping, by modulation doping or direct doping techniques, has been proposed to suppress QD-barrier thermal coupling and mitigate recombination loss [7,10,11]. Modulation doping is realized by incorporating δ-doping layers in the GaAs barrier spacers between the QD stacks [7,12], whereas direct doping [11,13] is implemented by incorporating dopant atoms in the InAs QDs during QD growth. Experiments have indeed demonstrated remarkable V_{oc} recovery using this approach, but the underlying mechanisms and their quantitative impact have not yet been completely assessed. At room temperature, V_{oc} preservation through non-equilibrium processes such as second photon absorption does not seem realistic since second photon induced escape rate is always found much lower than thermal and/or field assisted escape rate, even in directly doped QDs wherein two-photon absorption was observable at room temperature [11,14]. Substantial suppression of nonradiative recombination by QD

* Corresponding author.
E-mail address: federica.cappelluti@polito.it (F. Cappelluti).

doping has been inferred in several works: Concerning modulation-doped QDSCs, reduced dark current and improved V_{oc} over undoped samples were reported in Ref. [10]. Substantial V_{oc} recovery and slight reduction of J_{sc} were shown in Ref. [12] and were attributed, also on the basis of device level simulations, to reduction of nonradiative recombination and slightly decreased collection efficiency with respect to undoped cells. With regard to directly doped QDSCs, enhanced photoluminescence (PL), reduced dark current and increase of sub-gap photocurrent were reported in Ref. [11]. Emission properties of directly doped QDs were also studied in Ref. [15], demonstrating considerably improved PL and reduced thermal quenching. Improved QDSC efficiency with appropriate doping level has been demonstrated in Ref. [16], where high room temperature PL enhancement and V_{oc} recovery were achieved without J_{sc} reduction. Beyond an optimum doping level, concomitant reduction of PL and J_{sc} were measured. Somewhat in contrast with these results, [13] recently reported large V_{oc} recovery and PL enhancement in doped cells but nonradiative recombination was found to be increased with respect to undoped samples based on the observed degradation of J_{sc} and spectral response. The improvement of V_{oc} despite larger nonradiative recombination was explained by thermal decoupling between QD states and barrier, whose signature may also be the increase of PL intensity (measured at short circuit) with doping reported in Ref. [7] for modulation doped cells.

Overall, experimental results show that QD doping influences different aspects of the cell behavior, leading to conclusions that might appear, at least to some extent, even contrasting, and make it difficult to quantify the actual advantage that could be expected by the use of selective doping in high-quality crystal QDSCs. Crystal quality itself may be actually influenced by direct doping [13,16]. Moreover, besides QD selective doping, background doping was also shown to affect the device performance and need to be considered when interpreting experimental results [17]. The interpretation of photovoltaic, spectral and PL measurements in solar cell structures is complicated by the fact that doping locally affects QD carriers dynamics but also bulk carrier transport. In fact, carriers captured and escaping from the dots are subject to drift and diffusion across the barrier. Thus, the distribution of photogenerated carriers depends on the effective diffusion length which itself is dependent on features of the interdot layers, such as electrical field and recombination profile, that are modified by the

insertion of dopants. On the other hand, a reliable, even quantitative, assessment of how doping affects QD dynamics and photocarrier transport, and their interaction as well, is a key step towards the design of high efficient QDSCs.

In this paper, we present an extensive study on selectively doped QDSCs, using an *ad hoc* simulation approach, previously developed by some of the authors [8], that combines a drift-diffusion model for carrier transport in bulk layers with a detailed description of QD interband and intersubband carrier processes. The model was shown to well reproduce the measured characteristics of typical undoped InAs/GaAs QDSCs at room temperature [8]. We discuss here how short circuit and open circuit behavior are influenced by doping profile and density, depending on whether modulation or direct doping is used. A uniform doping situation is also studied, as a limit case representing devices where significant out-diffusion of doping might take place during the fabrication process, yielding a doping profile smoother than the nominal one [12] or even leading to significant, unintentional background doping of the interdot layers [17]. We assume QDs fabricated by optimized growth approaches, wherein significant changes to crystal quality induced by QD growth or selective doping may be discarded. Under this hypothesis, on the basis of the comparative analysis of undoped and doped cells, and of reference bulk cells as well, the inherent role of doping on QD recombination and charge transfer processes from one side, and on transport and collection efficiency from the other side, can be singled out. Doping influence is investigated in both radiative and nonradiative recombination limited barrier layers, by simulating photovoltaic characteristics, spectral response and PL properties, enabling to achieve a deeper understanding of the device physics and to establish a clear link with experimental results.

2. Method

2.1. Model

A sketch of the basic QDSC structure analyzed in this work is drawn in Fig. 1: N QD layers are uniformly stacked in the intrinsic GaAs region (hereinafter base) between the p-type emitter and the n-type back contact. Optimized devices will typically include widegap window layers as front and back surface fields and a bulk
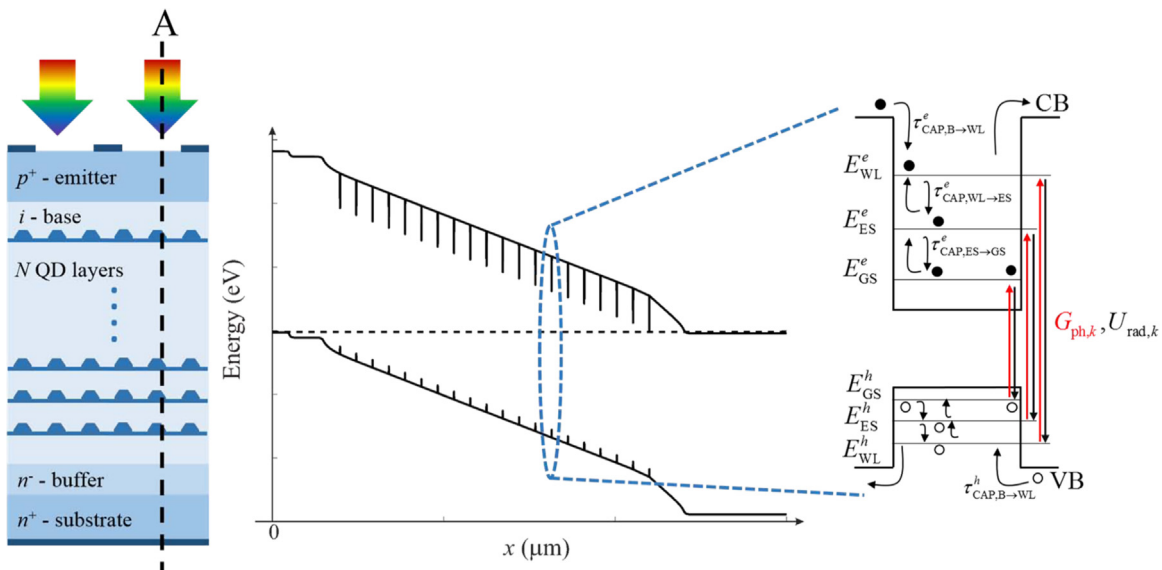

Fig. 1. Sketch of the studied GaAs p-i-n solar cell with embedded QD layers and the corresponding energy band diagram at thermal equilibrium along cutline A. On the right, QD energy states and interband and intersubband transitions considered in the model.

portion of the base. In this work, however, we keep the structure as simple as possible, but not simpler, to allow for clearly identifying the influence of doping on the QD medium and linking the analysis to the widest possible range of experimental results.

As summarized in Fig. 1, QDSCs are simulated with a numerical model that self-consistently includes a drift-diffusion description of carrier transport in the bulk material and a set of phenomenological rate-equations (REs) for QD carrier dynamics [8]. We briefly summarize here the most relevant aspects on the approach used to model the interband and intersubband carrier dynamics within a drift-diffusion-Poisson framework, while the detailed description of the model equations may be found in Ref. [8]. QDs are modeled as a three-level system, including electron/hole ground state ($GS^{e,h}$), excited state ($ES^{e,h}$) and the two dimensional WL state ($WL^{e,h}$). The REs include photogeneration in WL, ES and GS states, electron and hole capture from the GaAs barrier into the WL state, cascade relaxation process in the ES and GS, escape to the higher energy state, and recombination loss in the WL and confined states [8]. The intersubband electron and hole dynamics are modeled by characteristic scattering times (i.e. capture, relaxation and escape time constants). We assume that the escape from one state to the higher energy one only occurs via thermal effect, whereas tunnelling from confined to barrier states and escape via infrared photon absorption are neglected. Therefore, the thermal escape time constant from state k to higher energy state j ($\tau_{\mathrm{ESC},k\rightarrow j}^{e,h}$) is connected to the capture time constant from j to k ($\tau_{\mathrm{CAP},j\rightarrow k}^{e,h}$) by the detailed balance at thermal equilibrium:

$$\tau_{\mathrm{ESC},k\rightarrow j}^{e,h} = \frac{N_k^{e,h}}{N_j^{e,h}}\tau_{\mathrm{CAP},j\rightarrow k}^{e,h}\exp\left(\frac{\Delta E_{jk}^{e,h}}{k_{\mathrm{B}}T}\right). \tag{1}$$

being $N_{k(j)}^{e,h}$ the electron/hole density of states in the $k(j)$ state, and $\Delta E_{jk}^{e,h}$ the electron/hole energy separation between the two states. For ES and GS, $N_k^{e,h}$ is given by the per layer QD density, N_{QD}, multiplied by the state degeneracy factor, $g_k^{e,h}$. The WL state is also treated as a discrete state [18] with equivalent density of states $N_{\mathrm{WL}}^{e,h}$. Capture time constants are set in a phenomenological way, by comparison with experimental results [8]. In the present simulations we neglect the modification of the QD potential profile induced by the free carriers accumulated in the QDs and thus the capture/escape time constants are the same as in the undoped case. It is worth noticing that the reduced carrier confinement, as suggested from the GS blue-shift reported for selectively doped QDs (typically limited to a few meV [7,13]), would imply a decreased escape time and thus it would enhance rather than contradict the overall trends emerging from our analysis. Therefore, carrier capture and escape rates between j and k state are formulated as [8]:

$$R_{\mathrm{CAP},j\rightarrow k}^{e,h}|_i = \frac{N_j^{e,h}}{\tau_{\mathrm{CAP},j\rightarrow k}^{e,h}}f_j^{e,h}\left(1 - f_k^{e,h}\right)\Big|_i \tag{2a}$$

$$R_{\mathrm{ESC},k\rightarrow j}^{e,h}|_i = \frac{N_k^{e,h}}{\tau_{\mathrm{ESC},k\rightarrow j}^{e,h}}f_k^{e,h}\left(1 - f_j^{e,h}\right)\Big|_i \tag{2b}$$

being $f_{k(j)}^{e,h} = n_{k(j)}^{e,h}/N_{k(j)}^{e,h}$ the electron/hole occupation probability of state $k(j)$ with effective density of states $N_{k(j)}$, and i the index corresponding to the i-th QD layer.

The recombination loss in the QD states is assumed only due to radiative recombination, since we study here the effect of doping in an ideal, defect free, QD material. The radiative recombination in the QD k-th state reads as:

$$U_{\mathrm{rad},k}|_i = \frac{N_k}{\tau_{r,k}}\left(f_k^e f_k^h - f_{k,0}^e f_{k,0}^h\right), \tag{3}$$

where $f_{k0}^{e,h}$ are electron/hole occupation probabilities at thermal equilibrium. Occupation probabilities in Eqs. (2)–(3) are calculated through the self-consistent solution of the continuity equations for barrier carriers and the rate equations for charge transfer processes across the QD states, which are coupled through the escape (relaxation) rates of confined carriers towards (from) the barrier and the Poisson equation [8].

2.2. Analyzed structure and model parameters

We consider QDSCs embedding 20 layers of InAs QDs in a 1000 nm thick intrinsic layer (residual doping of 1×10^{13} cm^{-3}). QD density per layer is 6×10^{10} cm^{-2}. The cell has a p-i-n structure with p-type emitter made by a 50 nm p^+ GaAs contact layer with doping density of 5×10^{18} cm^{-3} and a 100 nm p GaAs layer with doping density 1×10^{18} cm^{-3}; 1000 nm intrinsic layer containing QDs; 50 nm intrinsic GaAs buffer layer and a 300 nm thick n^+ GaAs contact layer with doping density of 1×10^{18} cm^{-3}.

The QD optical photogeneration is modeled following [8]. Interband optical transitions are calculated from the absorption spectrum by accounting for electron and hole occupation in the QD states. The GS and ES absorption spectra have a gaussian shape centered at about 1.13 eV and 1.21 eV, with FWHM linewidth of 70 and 50 meV, respectively. The optical absorption of the WL state is modeled in analogy with the one of a quantum well layer [19]. The detailed wavelength dependence of the optical absorption is reported in Fig. S1 in the Supplementary Material. Model parameters for QD and WL states are summarized in Table 1.

The model includes barrier radiative recombination, with radiative coefficient set to 2.0×10^{-10} cm^3 s^{-1}, and defect induced non-radiative recombination modeled according to Shockley Read Hall (SRH) theory, with carrier lifetimes ranging from 500 ns (high quality material, close to the radiative limit) down to 1 ns (highly defective material). All the presented simulations are done at ambient Temperature, $T=300$ K.

To model the modulation and direct doping case, 5 nm thick δ-doping layers are placed in the middle of the GaAs spacer or at the QD layer, respectively. The sheet density of dopants is set to a multiple (α) of the QD density so as to nominally provide α carriers per dot. It is worth noticing that the actual QD filling depends on the interplay between drift-diffusion of free carriers in the bulk and net capture rate in the QDs and is therefore generally found to be non-uniform across the QD layers and different from the nominal per-dot doping density. In the uniform doping case, given a nominal per-dot doping density α, the dopant concentration is calculated by conserving the total (per-unit-area) dopant dose of

Table 1.
QD parameters.

QD density, N_{QD}, [cm^{-2}]	6×10^{10}
State degeneracy, $g_{\mathrm{ES}}^{e,h}$, $g_{\mathrm{GS}}^{e,h}$	4, 2
WL Density of States, $N_{\mathrm{WL}}^{e,h}$, [cm^{-2}]	2.4×10^{12}
$\Delta E_{\mathrm{B-WL}}^e$, $\Delta E_{\mathrm{WL-ES}}^e$, $\Delta E_{\mathrm{ES-GS}}^e$, [meV]	140, 62, 70
$\Delta E_{\mathrm{B-WL}}^h$, $\Delta E_{\mathrm{WL-ES}}^h$, $\Delta E_{\mathrm{ES-GS}}^h$, [meV]	4, 4, 16
$\tau_{\mathrm{CAP,B\rightarrow WL}}^e$, $\tau_{\mathrm{CAP,WL\rightarrow ES}}^e$, $\tau_{\mathrm{CAP,ES\rightarrow GS}}^e$, [ps]	0.3, 1.2, 1.2
$\tau_{\mathrm{CAP,B\rightarrow WL}}^h$, $\tau_{\mathrm{CAP,WL\rightarrow ES}}^h$, $\tau_{\mathrm{CAP,ES\rightarrow GS}}^h$, [ps]	0.1, 0.1, 0.1
τ_r^{WL}, τ_r^{ES}, τ_r^{GS}, [ns]	1, 1, 1
Peak optical absorption, α_{WL}, α_{ES}, α_{GS}, [cm^{-1}]	10^4, 900, 400
QD thickness, t_{QD}, [nm]	4

the δ-doped cells.

3. Results and discussion

To focus the ideas, we consider the calculated J-V characteristics shown in Fig. 2 for the reference GaAs cell, the undoped QDSC, and n- and p-type modulation-doped QDSCs, assuming SRH lifetime of 500 ns. The n-type modulation doped cell ($\alpha = 4$ e/dot) achieves a V_{oc} recovery of about 20 mV with respect to the undoped cell accompanied by a slight reduction of the J_{sc}, whereas the p-type modulation doping ($\alpha = 1$ h/dot) causes a pronounced reduction of J_{sc} and no recovery of V_{oc}. It might be worth reminding that in a bulk cell, similar V_{oc} recovery could be expected from p-type and n-type doping (see Fig. S2 in the Supplementary Material). Thus, the strong asymmetry of the QDSC behavior with respect to the doping polarity must be attributed to the QD radiative recombination and the markedly asymmetric dynamics of holes and electrons in the QD states [7]. As discussed in Ref. [20] based on steady state and transient simulations, fast hole dynamics (owing to the closely spaced QD valence band states) and efficient barrier transport are prerequisites to prevent recombination loss across the QDs allowing for high collection efficiency at short circuit and open circuit voltage preservation. QD hole filling impairs the fast hole dynamics and yields a substantial increase of QD capture and recombination loss. In fact, the additional holes accumulated in the QDs because of p-type doping, enhance recombination through the GS state of electrons photogenerated in the barrier or in higher energy QD states and then captured in the GS. Thus, the achievable J_{sc} is significantly reduced and at open circuit QD radiative recombination remains the main cause of V_{oc} reduction. Such behavior was experimentally observed in p-type modulation doped cells in Ref. [12], but an explanation was not provided; in fact, physics-based simulations reported in Ref. [12], would have predicted a slight photovoltage recovery, and of the same sign were also the conclusions in Ref. [21], wherein photovoltage was speculated to improve with doping regardless of whether n-type or p-type. Although the conclusions in [12,21] on the suppression of the SRH recombination by doping were correct, these works have not fully addressed the implications of the substantial asymmetry of electron and hole dynamics in QDs.

Restricting the analysis to the n-doping approach, it is worth to analyze how the cell behavior is affected by the per-dot doping
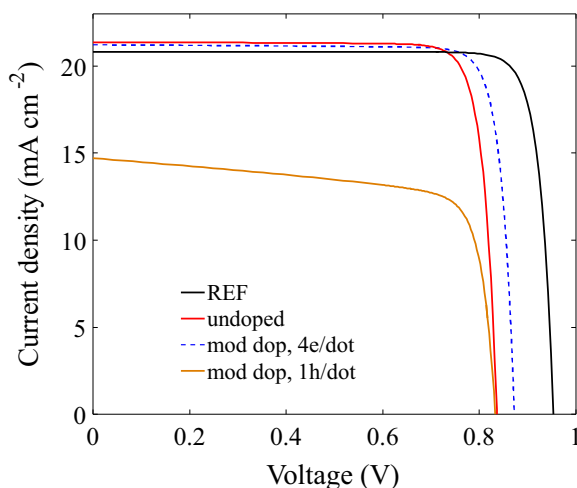

Fig. 2. $J - V$ curve of reference solar cell (with base residual doping of 1×10^{13} cm^{-3}), undoped QD cell, n-type modulation doped QD cell with nominal density of 4 e/dot, p-type modulation doped QD cell with nominal density of 1 h/dot, under 1 sun AM1.5G illumination.

density, considering the different doping profiles mentioned above, namely direct, modulation and uniform doping. Section 3.1 provides an overview of the results in terms of photovoltaic characteristics. In Sections 3.2 and 3.3 the discussion of short circuit and open circuit behavior is complemented by simulated spectral response and PL, and discussed by analysing the spatial variation of QD occupation and recombination rates across the cell.

3.1. Effect of doping profile and doping level on photovoltaic conversion efficiency

An overall assessment of the cell photovoltaic performance dependence on doping profile and density is presented in Fig. 3 considering bulk SRH lifetimes of 500 ns and 10 ns. For the sake of reference, the doping dependent behavior of the REF cell is also reported, showing the well known benefit of base doping in terms of V_{oc} recovery in defective bulk cells [22,23]. Since QDs act as traps at open circuit, in a similar way doping recovers the V_{oc} of QD cells. As first, we may notice that the undoped QD cells reach similar V_{oc} regardless of the SRH lifetime in the barrier, meaning that V_{oc} is limited by QD radiative recombination. The calculated trends highlight the effectiveness of doping in both the ideal and defective barrier case; the closeness of the curves points out that in the event of added defects induced by QD doping, V_{oc} recovery with respect to the undoped cell may still be appreciable. Comparable V_{oc} recovery is achieved by the different doping profiles, albeit a slight advantage of the modulation doping case is visible. At the highest doping density the estimated recovery ranges between 70 and 90 mV depending on the crystal quality and doping method. Even greater photovoltage improvement might be expected in QDSCs exploiting front and surface back fields, wherein minority carrier recombination at the contacts is suppressed. Although a detailed quantitative comparison is not possible at this time, given the general and simplified device structure under study, the simulated trends are in good agreement with literature, where experimental data on δ-doped cells range from a few mV in Ref. [7] up to 121 mV for the 8 e/dot modulation-doped cell in Ref. [12] (wherein also simulations were presented, with an estimated recovery of about 15 mV for the 8 e/dot cell), and 105 mV for the 18 e/dot directly doped cells in Ref. [13].

While in the high-quality bulk material ($\tau_{SRH} = 500$ ns), V_{oc} monotonically increases with the per-dot doping density, for the higher defective case ($\tau_{SRH} = 10$ ns) a slight dip of the V_{oc} curve is observed at low doping levels ($\alpha = 1$–2 e/dot, corresponding to 1.2–2.4×10^{16} cm^{-3} in terms of equivalent background doping). In contrast, in the reference bulk cell, doping always improves the V_{oc} owing to the shrinking of the depleted region and subsequent reduction of SRH recombination. As detailed in Section 3.3, the peculiar behavior of the QDSC at low doping levels arises from the modification of potential and carriers profiles across the cell which, whilst suppressing the radiative recombination through the QDs, enhance the SRH one across the neutral portion of the base. At high doping levels, the saturation of V_{oc} recovery attained by the QDSCs, even in the case of ideal barrier material, suggests that the main limiting factor still is QD radiative recombination, due to the onset of significant recombination through the WL state. As discussed later also on the basis of PL simulations, in the defective bulk cell ($\tau_{SRH} = 10$ ns), the dominant recombination mechanism limiting V_{oc} changes as the per-dot doping density increases: in the undoped or very low doping case ($\alpha < 1$ e/dot) the dominant recombination process is always radiative recombination through the GS; at $\alpha = 1 - 2$ e/dot, SRH recombination is the main one; at intermediate doping levels ($\alpha = 3 - 8$ e/dot) SRH and QD radiative recombination contribute to a similar extent, and finally, at higher doping levels ($\alpha > 8$ e/dot), QD recombination through the extended WL states
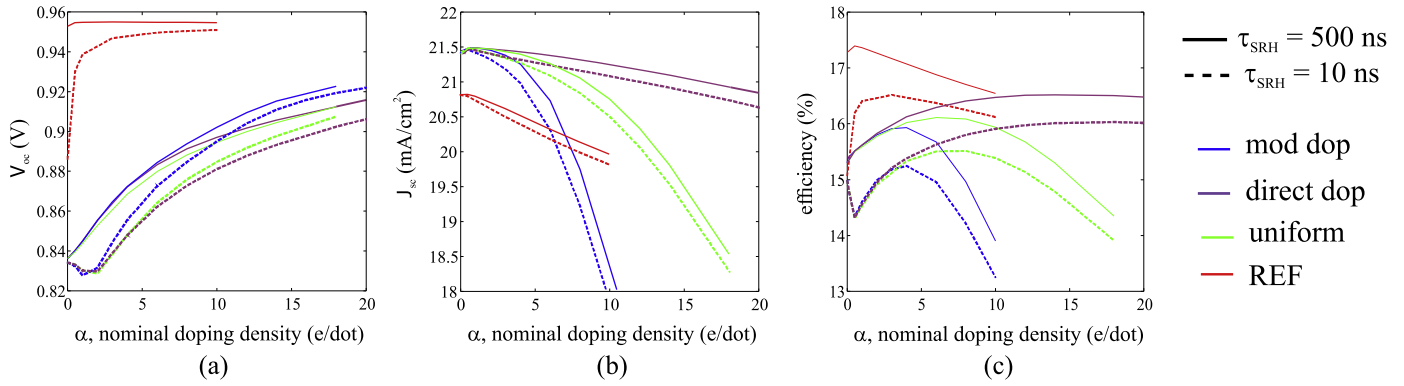
Fig. 3. Open circuit voltage (a), short circuit current density (b) and cell efficiency (c) as a function of the nominal per dot doping density for the *n*-type QD cells exploiting modulation, direct and uniform doping, assuming a high quality barrier (τ_{SRH} = 500 ns, solid lines) and a defective barrier (τ_{SRH} = 10 ns, dashed lines), obtained under 1 sun AM1.5 G illumination.

turns to be the dominant recombination mechanism. Since the underlying mechanism is essentially a competition between different loss channels, the indicated values of the per-dot doping density for the onset of the different regimes of recombination, and the sensitivity to unintentional background doping as well, depend on the time constants characterizing the QD charge transfer processes, and thus on specific QD features such as size and shape.

V_{oc} recovery is always accompanied by a decrease of J_{sc} (more pronounced in the modulation doping case) the more relevant, the greater bulk SRH recombination is. Such a behavior is common to all the investigated cells included, as well known, the REF bulk cell. The observed reduction is not the consequence of any additional defect (not included in the model) but rather of the shrinking of the base drift region. In fact, when the base is *n*-doped, the junction shifts towards the p^+ contact, increasing the length in the

neutral region across which photogenerated carriers need to diffuse before being collected at the contacts. Thus, the J_{sc} penalty is due to a decreased collection of carriers [12]. The amount of J_{sc} reduction as the doping level increases is however strongly affected by the presence of QDs and by the specific doping profile, as discussed in detail in Section 3.2.

V_{oc} recovery and J_{sc} degradation yield a trade-off in terms of achievable efficiency as a function of per-dot doping density. The maximum efficiency is found at increasingly higher doping levels for the modulation (4 e/dot), uniformly (8 e/dot), and directly (18 e/dot) doped cells, with an absolute improvement with respect to the minimum observed at α=1–2 of 0.9%, 1.2%, and 1.7% respectively. Higher efficiency improvement could be within reach in optimized designs, with larger base thickness, optimum placement of the QD layers and use of window layers. Overall, the analysis confirms selective doping as a good strategy for
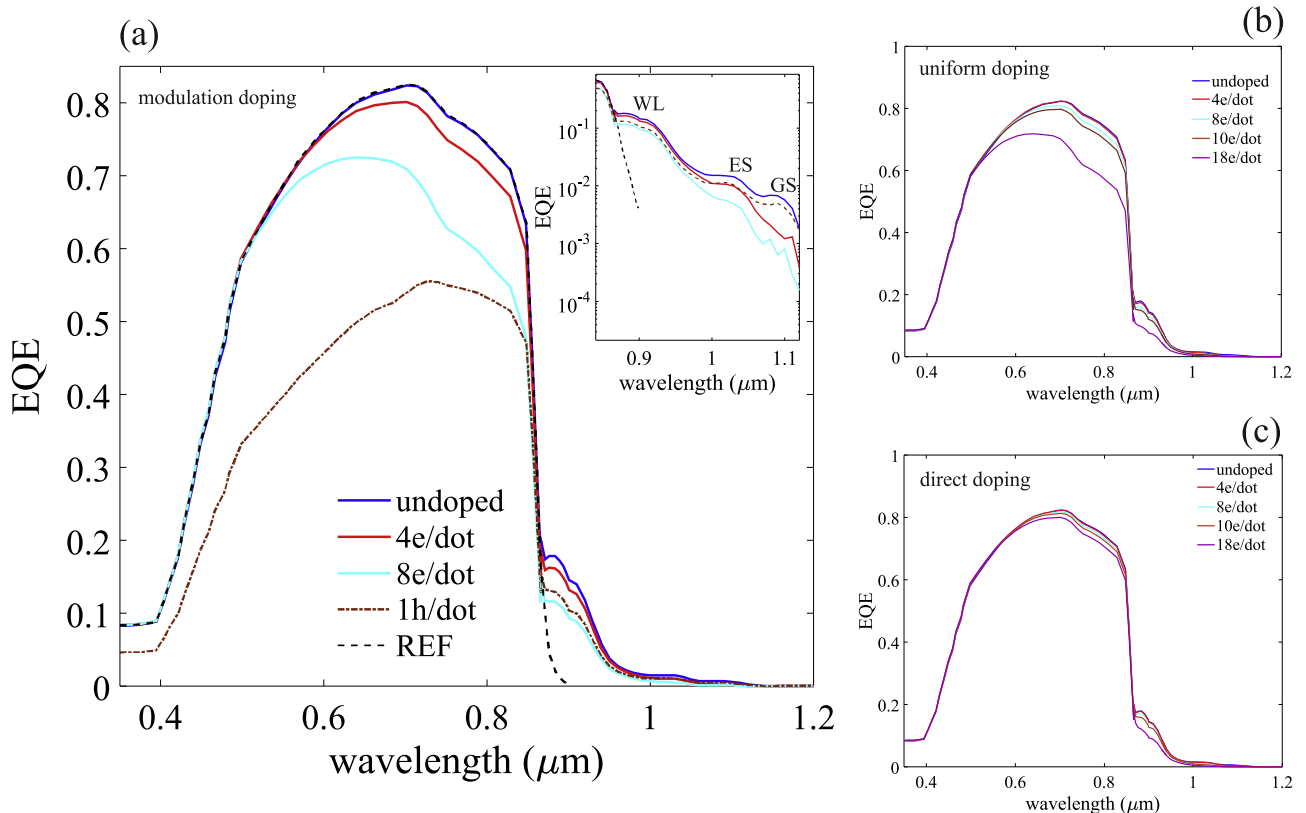

Fig. 4. External Quantum Efficiency (EQE) spectra for (a) modulation doped, (b) uniformly doped, and (c) directly doped QDSCs. The inset in figure (a) shows a zoom of the EQE spectra in the sub-bandgap region.

optimizing QDSC design where, coupled with light trapping techniques, it would allow to overcome the efficiency of the reference cell.

3.2. Short circuit condition

The observed J_{sc} degradation is further substantiated by the EQE spectra reported in Fig. 4, that show how the reduction of photocurrent response in the above-gap region for the same nominal per-dot doping level is affected by the specific doping profile. In particular, the penalty within the 600–800 nm wavelength range points out increased recombination in the base region due to the degradation of carriers effective diffusion length and turns to be very sensitive to the doping method. As assessed later on the basis of the analysis of the energy band diagram and QD occupation probability, the degradation of the diffusion length is due to the modulation of the potential and electric field profiles in the base interdot regions, that hinder the transport of free carriers escaping from the QDs or photogenerated in the barrier, yielding an increased recombination through QDs. The limited EQE degradation at increasing doping density in directly doped cells is well matched with the experimental trend observed in [13] for 6–18 e/dot directly doped cells, while a larger change is observed for the modulation doping case in qualitative agreement with [12]. Also the reference cell, coherently with the J_{sc} penalty observed in Fig. 3(b), shows a significantly reduced EQE in the 600–800 nm wavelength region (see Fig. S2 in the Supplementary Material), causing a penalty of J_{sc} of about 10% at 18 e/dot. This suggests that the EQE degradation reported in Ref. [13] for the 18 e/dot bulk cell with respect to both undoped bulk and QD cells, could be largely attributed to the inherent behavior of the cell and to a lesser extent to doping induced formation of defects. On the other hand, point defects, together with a possible non negligible out-diffusion of dopants (as suggested by the larger change in the EQE predicted for the uniformly doped cell in Fig. 4(b)) need to be called for to explain the degradation of the directly doped QDSCs in [13] with respect to the undoped ones.

Finally, Fig. 4 highlights the change in sub-gap EQE induced by the QD doping (somewhat less sensitive in this case to the specific doping profile). EQE suppression at the longest wavelengths reflects the electron filling of ES and GS states and the subsequent suppression of optical transitions, while the EQE decrease in the WL wavelength range can again be attributed to a decreased collection efficiency. The resulting picture is in good agreement with the analysis in [12,13] for modulation and directly doped cells, respectively.

The impact of doping on the collection efficiency is well understood by analysing how the δ-doping layers affect barrier transport and QD carrier filling. To this aim we restrict the analysis to the modulation doped cell, referring the reader at the synoptyc figures in the Supplementary Material for the other doping profiles. The energy band diagrams at short circuit condition, under AM1.5G illumination, for the undoped and modulation doped cells are compared in Fig. 5.

In the undoped cell, the base is characterized by a high and almost constant electric field that favours the efficient transport of photogenerated carriers towards their respective contacts. On the contrary, the base of the modulation doped cell presents two well defined regions: one region with large band bending towards the *p* emitter (corresponding to the depleted region that onsets at the *p-n* junction formed by the emitter itself and the first delta-doping layer) and one region with flat energy bands, characterized by a periodic space modulation of the potential, which extends across the base towards the *n* contact. The depletion region that arises in the interdot layers due to transfer of free carriers from the δ-
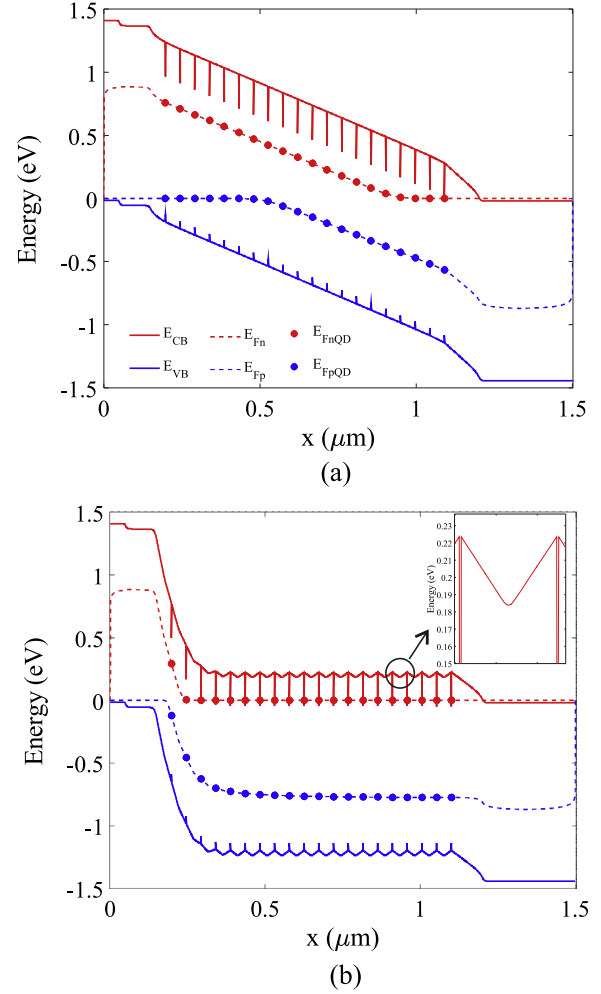

Fig. 5. Energy band diagram at short-circuit condition for the undoped (a) and the 4 e/dot modulation doped cell (b).

doping layers into the QDs (see zoom in the inset of Fig. 5(b)), induces the formation of potential barriers and wells in the conduction and valence band, respectively [24], which prevent capture of electrons but at the same time promote capture of holes in the QDs. Barrier and well height is found to be proportional to the doping concentration with a value of about 10α meV.

The corresponding QD carrier filling is reported in Fig. 6: *n*-doping increases the electron filling of all the QD layers; hole filling decreases in the QD layers next to the junction while it increases by about two orders of magnitude in the QD layers placed in the flat band region (from a depth of 0.5 μm towards the *n*-contact). The increment of QD electron and hole density in the flat-band region turns into enhanced radiative recombination rate that become competitive against the carrier escape rate out of the QDs. Fig. 7(a)–(b) shows the corresponding spatial distribution of photogeneration, net escape rate ($R_{ESC} - R_{CAP}$) from the WL to the bulk, and recombination paths through the QD and bulk states. Positive net escape indicates that the QD carriers are extracted out of the QD layer, negative escape rate indicates that the QDs act as capture (or trap) centers. The comparison against the undoped cell points out that in the doped cell QD layers placed in the flat band region poorly contribute to the total J_{sc}, since net escape rate is much smaller than QD photogeneration. In Ref. [20] we have shown that this occurs whenever the bulk hole sweep-out is impaired, as it does happens in this case due to the potential wells arising in valence band, that tend to confine holes within the QD capture range. Finally, QD radiative recombination turns to be
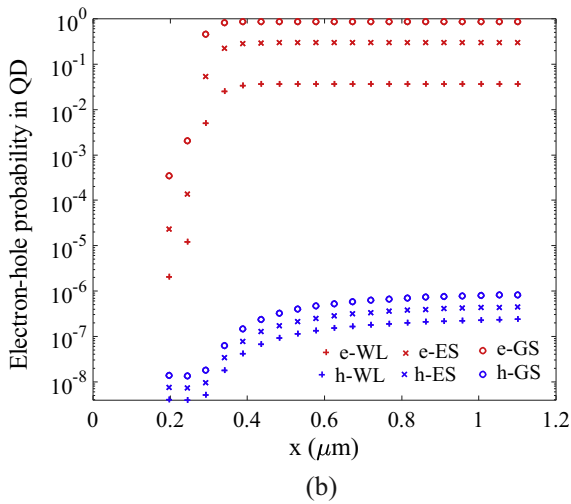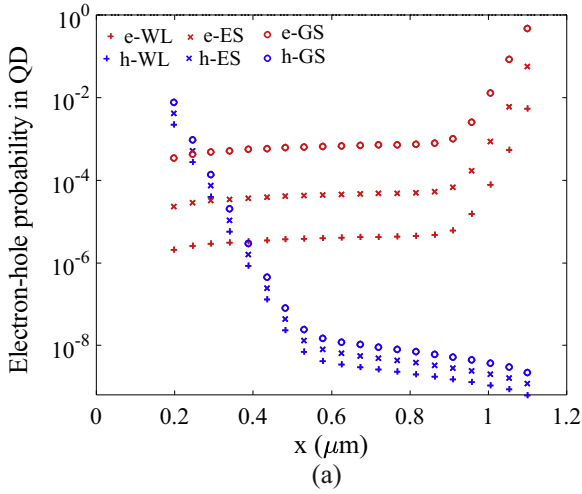
(a)

(b)

Fig. 6. Occupation probability of electrons (red) and holes (blue) in the QD states across the base at short-circuit for the undoped cell (a) and the 4 e/dot modulation doped cell (b). (For interpretation of the references to color in this figure legend, the reader is referred to the web version of this article.)
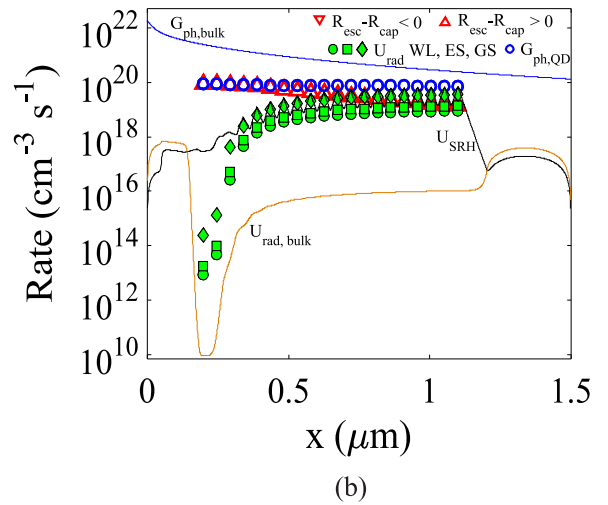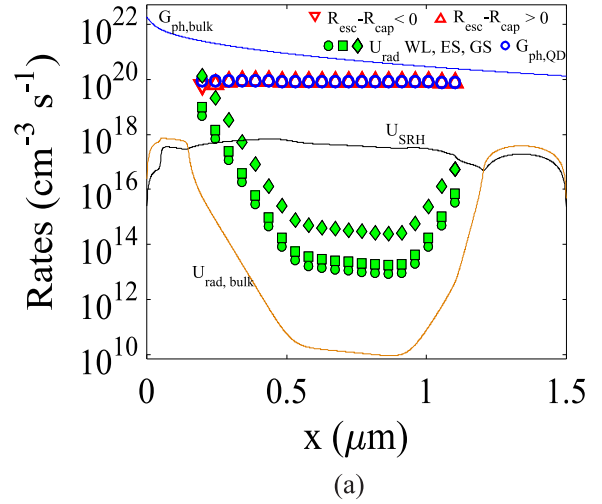

(a)

(b)

Fig. 7. Spatial distribution of photogeneration, net escape, and recombination rates at short-circuit for the undoped cell (a) and the 4 e/dot modulation doped (b) cell. The equivalent volume rates for QD states are computed by normalizing the corresponding surface rates by the QD layer interspacing (47 nm).

enhanced in the flat band region as a consequence of the effect of δ-doping on the QD state occupation distribution. Similarly, also the bulk SRH recombination profile peaks towards the n-contact, due to the modification of free carrier distribution and electric field induced by the modulation doping (see also Figs. S3–S4 in the Supplementary Material). As a result, in the QD layers close to the n-contact, QD photogeneration and radiative recombination almost equilibrate each other, yielding the decrease of the sub-gap photocurrent contribution seen in Fig. 4(a), while enhanced bulk SRH and QD radiative recombination are responsible for the observed degradation of the above-gap EQE.

If the doping density is further increased, the QD layers turn into effective recombination centers for carriers photogenerated in the barrier and become the dominant recombination mechanism in the flat band region. This yields the increasingly large J_{sc} penalty observed in Fig. 3 at increasing per-dot-density, regardless of the bulk SRH lifetime. PL measurements at short-circuit can be used to quantify the overall impact of carrier loss through the QD recombination channels [7]. The enhancement of QD recombination at high doping levels is revealed by the dependence of the short-circuit integrated PL intensity on doping density, as shown in Fig. 8. The GaAs barrier is excited with a monochromatic light at 532 nm and an excitation intensity of 1.1 W/cm². As shown in the
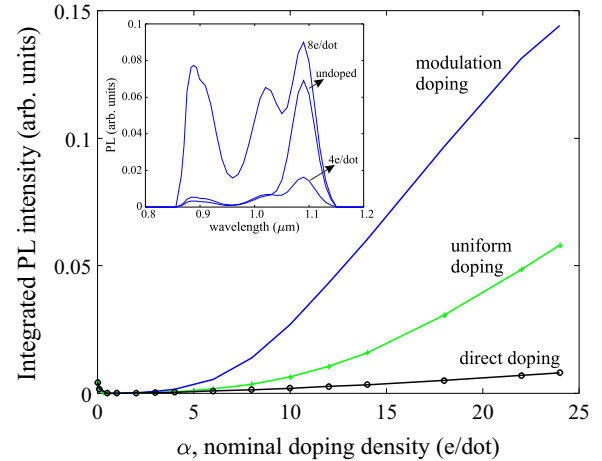

Fig. 8. Integrated PL intensity at short circuit condition as a function of the nominal per dot density for the different doping profiles. The inset shows the calculated PL spectra for the undoped cell, and the 4 e/dot and 8 e/dot modulation doped cells.

inset of Fig. 8, PL spectra are recorded in the wavelength range of QD emission including photoluminescence from GS, ES and WL. At low doping levels, $\alpha < 5$, the PL is slightly quenched due to the

dominant SRH recombination in the neutral base, as previously discussed for the 4 e/dot modulation doped cell. At higher doping levels, a large enhancement is observed for the modulation and uniform doping cases, whereas this enhancement remains quite limited for the direct doping case. Ideally, to preserve the J_{sc}, the QDs should present the smallest possible luminescence after exciting the bulk because photoexcited carriers should be removed by the barrier towards the contacts before being captured in the QDs. This is indeed true in both the undoped and directly doped cells, whose PL intensity is extremely small in comparison to the modulation and uniformly doped cases for the same doping level. The valence band wells arising in the modulation and uniformly doped structure promote the accumulation of holes in the QD region yielding reduced escape towards the barrier and increased recombination. On the other hand, in directly doped cells, the energy band profile is not significantly affected and holes remain delocalized across the barrier, since doping is almost confined within the QD layer. In this case, hole filling comparable to the one found in the 4 e/dot modulation doping case, and thus comparable PL emission, requires more than triple doping density (for a comparison, see the occupation probability distributions in Figs. S4–S5 of the Supplementary Material).
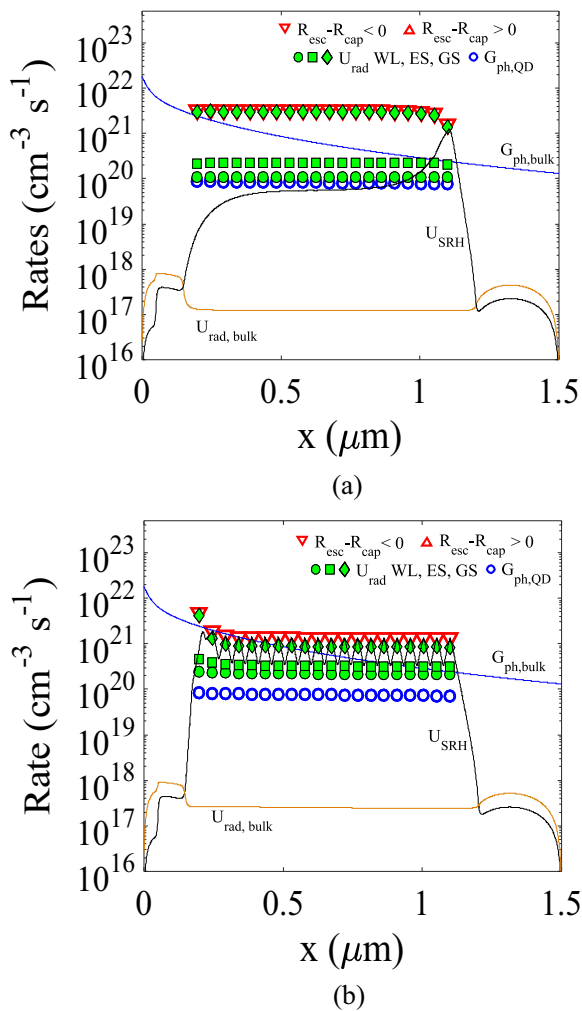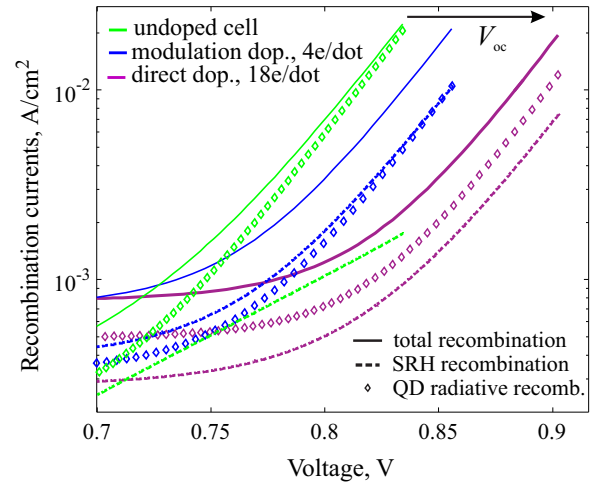

Fig. 10. Voltage dependence of the integrated recombination rates across the base region for the undoped, 4 e/dot modulation doped, and 18 e/dot directly doped cell: symbols are the recombination in the QD layers, $U_{rad,QD}$, dashed lines indicate the SRH recombination in the barrier, U_{SRH}, and solid lines the total recombination rate $U_{TOT} = U_{rad,QD} + U_{rad} + U_{SRH}$ (note that U_{rad}, not shown here, is always negligible across the base region). The voltage sweeps up to the V_{oc} of each cell, i.e. about 0.83 V, 0.85 V and 0.9 V for undoped, modulation doped and direct doped cell, respectively.

3.3. Open circuit condition

Fig. 9 compares the open-circuit spatial distribution of bulk recombination and QD capture and recombination rates for the undoped and 4 e/dot modulation doped cells. In both devices, at open circuit, QDs act as effective capture centers ($R_{ESC} − R_{CAP} < 0$). In the undoped device, recombination is dominated by QD radiative recombination through the GS across the whole base except for the QD layer next to the n-contact, wherein the peak of the electrical field maximizes the SRH bulk recombination. The displacement of the junction towards the n-contact, despite the base being intrinsic, is again a result of the large asymmetry between the QD electron and hole dynamics. Under forward bias condition, a large amount of electrons are captured in the QD states while holes, owing to their fast escape rate, remain almost free and delocalized across the barrier. Thus, the barrier is rich of free holes and the junction is displaced towards the n-contact. In the modulation doped cell, we observe a reduction of GS radiative recombination and an increase of bulk SRH such that the two rates become comparable and limit the V_{oc} at the same extent. SRH recombination is quite uniform across the whole base with a slight peak towards the p-contact. Finally, we observe a slight onset of ES and WL recombination.

To better understand how doping allows for photovoltage recovery, we analyze in Fig. 10 the QD radiative and SRH recombination rates (integrated over the base) as the voltage changes from the maximum power point (around 0.7 V for all the devices) up to V_{oc}.[1] In the undoped cell, the dominance of QD radiative recombination across the neutral part of the base shows up with an almost unitary ideality factor of the total recombination current, whereas the small SRH recombination contribution, being confined to the depleted region, is characterized by a larger ideality factor. For the undoped cell, V_{oc} is limited at about 0.83 V by QD radiative recombination. At this voltage, the modulation doped

(a)

(b)

Fig. 9. Spatial distribution of photogeneration, net escape, and recombination rates at open circuit for the undoped cell (a) and the 4 e/dot modulation doped (b) cell. The equivalent volume rates for QD states are computed by normalizing the corresponding surface rates by the QD layer interspacing (47 nm).

---

[1] It is worth mentioning that while the behavior of the integrated recombination rates at high voltage, when the cell operates close to flat-band condition, provides a straightforward means to assess the loss mechanisms of injected carriers, the same does not apply at low voltages, when the overall charge balance across the cell is significantly affected by the gradient of the carriers current components.
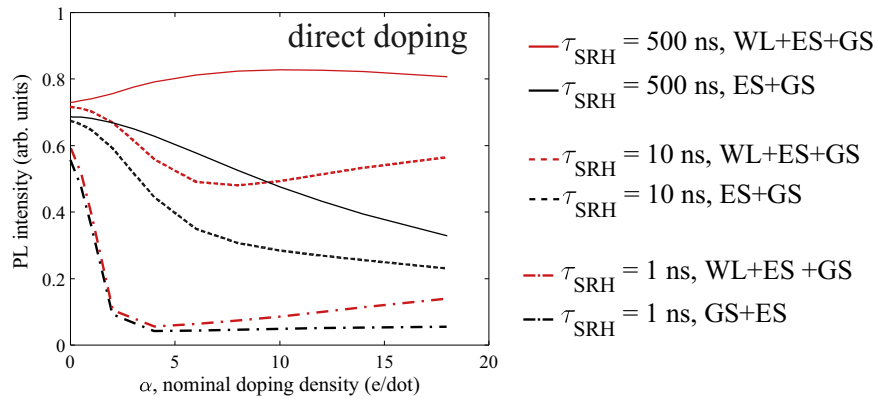
Fig. 11. Integrated PL intensity at open circuit condition as a function of the nominal per-dot doping density for the direct doping strategy, considering various SRH lifetimes.

cell shows suppressed QD recombination, thus a higher V_{oc} is attained. The V_{oc} achieves the value of 0.85 V and is limited by both SRH and QD radiative recombination. Note in fact that now, due to the flat SRH profile across the base observed in Fig. 9(b), also the SRH equivalent recombination current increases with an almost unitary ideality factor. Finally, the voltage dependence of the integrated recombination rates for the 18 e/dot directly doped cell is reported, showing a V_{oc} recovery of about 70 mV with respect to the undoped cell. Due to the higher doping density, at voltage values corresponding to the V_{oc} of the undoped and modulation-doped cells, the directly doped cell shows greatly suppressed radiative and SRH recombination. Radiative recombination is blocked by the GS carrier filling, while SRH recombination is kept small because of the slight barrier potential profile modification. When the cell reaches the V_{oc} of about 0.9 V, QD radiative recombination through the WL is the main recombination channel. It is worth mentioning that while the behavior of the integrated recombination rates at high voltage, when the cell operates close to flat-band condition, provides a straightforward mean to assess the loss mechanisms of injected carriers, the same does not apply at low voltages, towards short circuit, when the overall charge balance across the cell is significantly affected by the gradient of the carriers current components (i.e. the Quasi-Fermi levels).

A systematic analysis of the open circuit PL intensity as a function of the per-dot doping density has been carried out for the different doping profiles, by considering three possible scenarios in terms of barrier material quality, modeled by using SRH lifetimes of 500 ns, 10 ns, and 1 ns. The PL excitation is set as in the previous study at short circuit. Since very similar trends are observed for all the doping profiles, we report in Fig. 11 only the results for the direct doping case, and we refer the reader to Fig. S7 in the Supplementary Material for the other case studies. To help the discussion, besides the overall integrated PL intensity (including emission from all the QD states) also the contribution from the GS and ES states only is singled out. It is seen that the trends of the integrated PL (IPL) intensity with doping density are very much dependent on the SRH recombination lifetime, because the introduction of doping changes the amount but also the balance between SRH and radiative loss. For negligible SRH recombination ($\tau_{SRH} = 500$ ns) and regardless of the doping method, the IPL intensity versus doping level reaches a maximum and then slightly decreases. The maximum is due to the onset of significant radiative recombination through the WL state, whereas radiative recombination in the GS and ES is almost quenched by the blocking of electron capture in these states (already filled by the doping induced free electrons). This means that in the ideal bulk material case, the achievable photovoltage will be ultimately determined by carrier capture and recombination through the WL. For shorter bulk SRH lifetime ($\tau_{SRH} = 10$ ns) the undoped cell maintains the PL

intensity as high as in the high quality material case, indicating once again QD radiative recombination as the dominant V_{oc} degradation factor. In contrast, with dopant insertion, the PL intensity is initially quenched to a minimum value for $\alpha = 8$ e/dot and then starts to increase with the doping density owing to the onset of WL emission. The observed PL minimum is due to the predominance of the SRH channel loss against QD capture/radiative processes. As doping is further increased, WL emission becomes predominant over ES and GS emission and SRH recombination as well. Thus, WL recombination might remain an important cause of V_{oc} degradation even in cells with significant SRH recombination.

Finally, in the case of highly defective barrier material ($\tau_{SRH} = 1$ ns), besides a visible quenching of the PL already present in the undoped cell, it is interesting to observe the strong PL quenching in the doped cells that appears at low doping density. The PL minimum is displaced at lower doping levels ($\alpha = 2$–3 e/dot) and the intensity is attenuated of about one order of magnitude with respect to the undoped case, indicating a strong prevalence of SRH recombination. Taking into account that in the investigated devices such low values of α may be correlated to an unintentional background doping of about 10^{16} cm^{-3}, this result suggests that background doping of the interdot layers must be carefully considered when interpreting open circuit PL measurements, since it may significantly impact the recombination mechanisms. Summarizing, in devices with non negligible non-radiative recombination we may identify three ranges of doping levels (due to background doping or selective doping) characterized by a different mechanism that ultimately limits the attainable photovoltage: in purely undoped cells V_{oc} is always limited by radiative recombination through the GS/ES states; at intermediate doping levels V_{oc} is limited by SRH recombination, and finally, at high doping levels, QD radiative recombination through the WL state becomes the dominant mechanism. Thus, combining selective doping techniques with WL reduction [25,26], a larger thermal decoupling between barrier and QD is expected (also in high-quality crystals) and a larger V_{oc} recovery should be achievable.

The interplay between the SRH and QD radiative recombination gives rise to significant nonlinear behavior with respect to the PL excitation intensity. Fig. 12(a) analyses in detail the PL behavior with respect to the per-dot doping density of the directly doped cell for $\tau_{SRH} = 10$ ns and $\tau_{SRH} = 1$ ns and different excitation power densities. By decreasing the PL excitation from 1.1 W/cm^2 down to 0.1 W/cm^2, the IPL quenching at low doping levels is enhanced and so is the subsequent increase of the IPL with doping due to the emission from the WL states. The suppression of GS and ES emission and the concomitant enhancement of WL emission as doping density increases is highlighted in the PL spectra in Fig. 12 (b)–(c). In the highly defective case ($\tau_{SRH} = 1$ ns), the IPL minimum
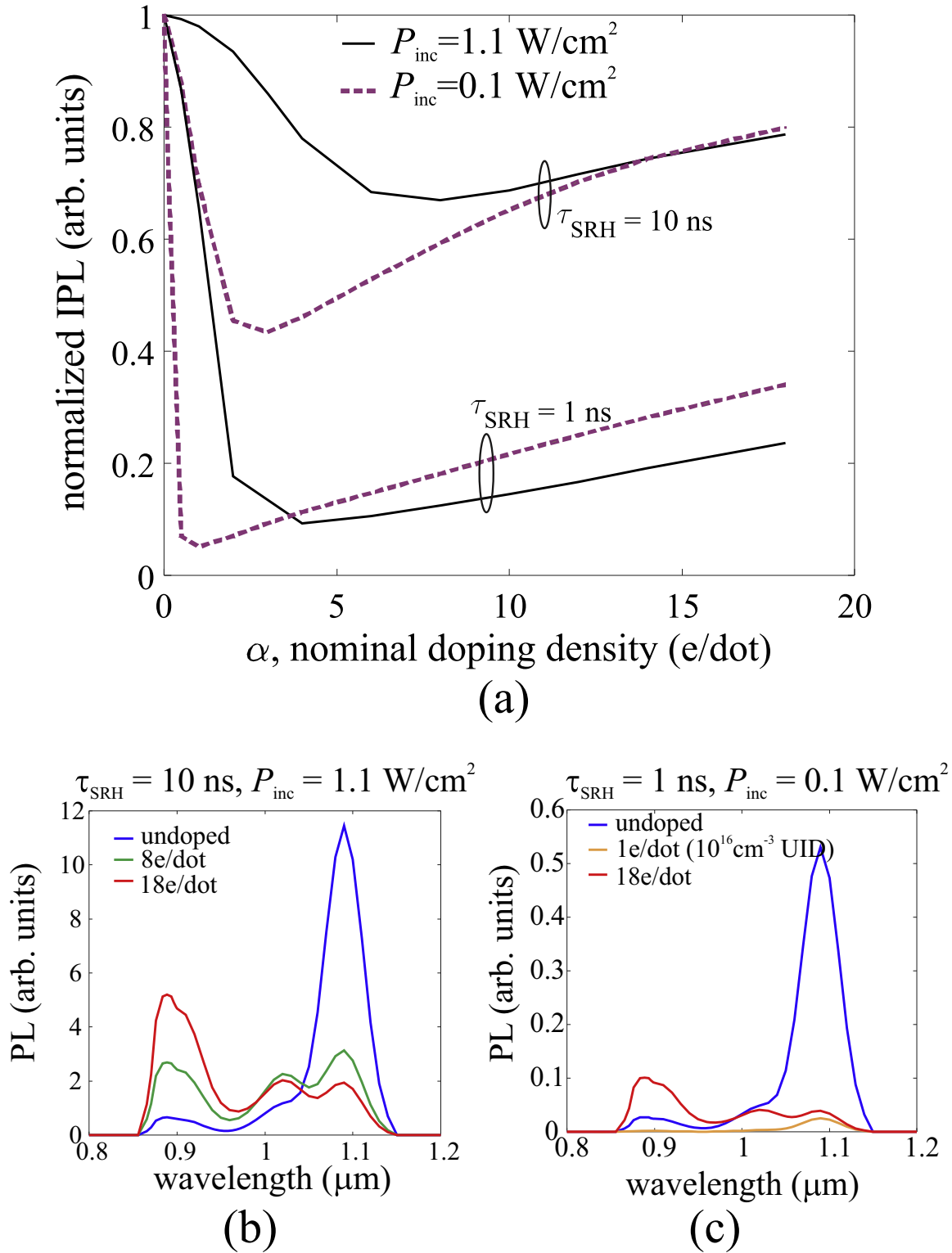
Fig. 12. (a) Normalized integrated PL intensity as a function of the nominal per-dot doping density for the directly doped cell with τ_{SRH} of 10 ns and 1 ns, under two different excitation intensities. (b) PL spectra at P_{exc} = 1.1 W/cm^2 for the undoped, 8 e/dot (corresponding to the minimum IPL), and 18 e/dot when τ_{SRH} = 10 ns. (c) PL spectra at P_{exc} = 0.1 W/cm^2 for the undoped, 1 e/dot (corresponding to the minimum IPL), and 18 e/dot when τ_{SRH} = 1 ns. As discussed in the main text, the 1 e/dot case may also be considered representative of a cell with background unintentional doping (UID) of about 10^{16} cm^{-3}.

shifts at doping density as low as $\alpha=1$ e/dot and then the IPL increases of about nine times when $\alpha=18$ e/dot. The observed behavior is in agreement with the PL measurements reported in Ref. [13], assuming a non negligible background doping in the undoped cell, and provides theoretical support to the interpretation of the PL enhancement in the doped cells as the result of reduced capture

and thermal decoupling between wetting layer and QD at high doping levels. In the present simulations, the effect results from the filling of GS and ES states and the consequent blocking of relaxation from WL states into QD confined states, since energy level spacings are unchanged with respect to the undoped case. Moreover, energy potential barriers induced by doping at the QD/
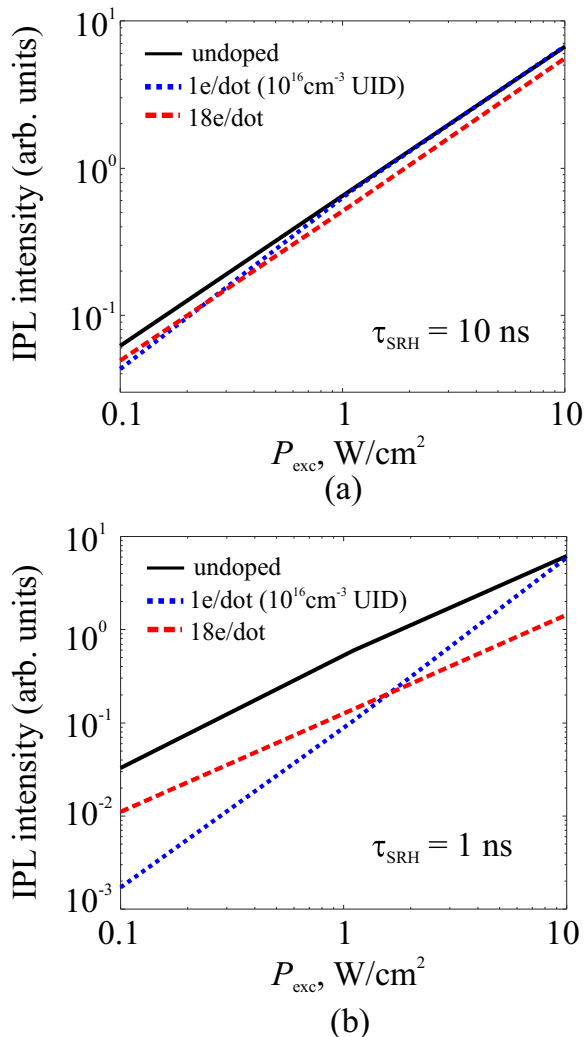
Fig. 13. Integrated PL intensity as a function of the excitation power density for undoped and directly doped cells with barrier SRH lifetime of 10 ns (a) and 1 ns (b).

barrier interface result to be limited to a few meV.

The dependence of IPL intensity on excitation power density for the undoped, 1 e/dot and 18 e/dot directly doped cells is reported in Fig. 13. For high-quality crystal cells (not shown here) we verified a linear behavior of the IPL intensity vs. excitation density and almost coincident IPL values, regardless of the doping level. In the defective bulk cases, the undoped and 18 e/dot cell, dominated by QD radiative recombination, show a linear behavior of the IPL with excitation intensity (i.e. unitary slope in both the log-log plots in Fig. 13). In contrast, the 1 e/dot cell, dominated by SRH recombination, shows a superlinear behavior (i.e. a slope of about 1.8 in the log-log plot) across the whole range of excitation power when $\tau_{SRH} = 1$ ns (Fig. 13(b)), and a change of behavior, from slightly superlinear at low excitation (slope of about 1.2) to linear at higher excitation, when $\tau_{SRH} = 10$ ns (Fig. 13(a)). Similar results were reported for directly doped QDs in Ref. [15] and for modulation doped QDs with dot-in-a-well structure in Ref. [27]: superlinear excitation dependence of PL intensity was observed in undoped QDs, whereas doped QDs showed an almost linear behavior. The change in excitation power dependence was explained in Ref. [15] by the effectiveness of QD doping in inactivating nonradiative recombination, while [27] attributed it to a change in the dynamics of electrons and holes in QDs (from uncorrelated dynamics in the undoped QDs to correlated dynamics in the doped QDs) due to enhanced Coulomb attraction induced by the excess carriers in the dots. In Ref. [28], by studying undoped QDs confined in an AlAs/GaAs superlattice which inhibited transport of carriers in the barrier, it was already suggested that independent e-h dynamics is at the root of the onset of superlinear dependence on excitation power. It is worth noting that our model indeed assumes independent e-h dynamics in the dots but, according to the results, the space-charge and barrier transport are the factors that ultimately correlate the e-h pair dynamics. According to our simulations, the superlinearity is actually triggered by the presence of defects which affect the diffusion across the barrier [29], at least as long as barrier transport exists. Thus, the change from superlinear to linear dependence of the IPL intensity on excitation power density induced by selective doping can be interpreted as a signature of suppressed nonradiative recombination.

4. Conclusions

We have presented an extensive study of selectively doped QDSCs, based on an advanced simulation tool that allows to describe in a comprehensive and self-consistent way barrier transport and QD carrier dynamics. We have clarified that the negative impact of *p*-type doping on the achievable V_{oc} observed in high-quality crystal samples is due to the asynchronous and faster dynamics of holes with respect to electrons. The impact of *n*-type doping on the photovoltaic characteristics has been addressed under different scenarios of barrier material quality. Improved power conversion efficiency with respect to undoped cells is predicted, despite a degradation of short circuit current, thanks to a remarkable V_{oc} recovery. In high quality crystals, photovoltage is recovered thanks to the suppression of capture and recombination through the QD confined states, whereas in defective crystals the recovery is the result of suppression of both nonradiative and radiative loss channels. In both cases, at high doping density, relaxation and recombination through the WL remains as the ultimate factor limiting the cell photovoltage. The competition between QD radiative and barrier nonradiative recombination causes a strong sensitivity to the background doping of the QD region and gives rise to significant nonlinear behavior of the integrated PL intensity with respect to the excitation power density. We finally demonstrate that the superlinear behavior is a footprint of dominant nonradiative recombination, whereas radiatively limited cells, despite the assumed uncorrelated electron and hole dynamics, show a linear behavior. Overall, the study presented here provides a coherent interpretation of the various results reported in literature and a deeper insight on the device-level changes induced by doping in view of designing high efficiency QDSCs.

Acknowledgements

Appendix A. Supplementary data

Supplementary data associated with this article can be found in the online version at http://dx.doi.org/10.1016/j.solmat.2016.05.049.

References

[1] A. Luque, A. Martí, Increasing the efficiency of ideal solar cells by photon in-duced transitions at intermediate levels, Phys. Rev. Lett. 78 (26) (1997) 5014–5017.

[2] Y. Okada, N.J. Ekins-Daukes, T. Kita, R. Tamaki, M. Yoshida, A. Pusch, O. Hess, C.C. Phillips, D.J. Farrell, K. Yoshida, N. Ahsan, Y. Shoji, T. Sogabe, J.-F. Guillemoles, Intermediate band solar cells: recent progressand future directions, Appl. Phys. Rev. 2 (2) (2015) 021302.

[3] J. Wu, S. Chen, A. Seeds, H. Liu, Quantum dot optoelectronic devices:lasers, photodetectors and solar cells, J. Phys. D: Appl. Phys. 48 (36) (2015) 363001.

[4] S. Turner, S. Mokkapati, G. Jolley, L. Fu, H.H. Tan, C. Jagadish, Periodic dielectric structures for light-trapping in ingaas/gaas quantum well solar cells, Opt. Express 21 (S3) (2013) A324–A335, http://dx.doi.org/10.1364/OE.21.00A324.

[5] A. Mellor, A. Luque, I. Tobías, A. Martí, The feasibility of high-efficiency inas/gaas quantum dot intermediate band solar cells, Sol. Energy Mater. Sol. Cells 130 (2014) 225–233.

[6] G. Wei, K.-T. Shiu, N.C. Giebink, S.R. Forrest, Thermodynamic limits of quantum photovoltaic cell efficiency, Appl. Phys. Lett. 91 (22) (2007) 223507.

[7] A. Sablon, J.W. Little, V. Mitin, A. Sergeev, N. Vagidov, K. Reinhardt, Strong enhamcement of solar cell efficiency due to quantum dots with built-in charge, Nano Lett. 11 (2011) 2311–2317.

[8] M. Gioannini, A. Cedola, N. Di Santo, F. Bertazzi, F. Cappelluti, Simulation of quantum dot solar cells including carrier intersubband dynamics and trans-port, IEEE J. Photovolt. 3 (4) (2013) 1271–1278, http://dx.doi.org/10.1109/JPHOTOV.2013.2270345.

[9] C.G. Bailey, D.V. Forbes, S.J. Polly, Z.S. Bittner, Y. Dai, C. Mackos, R.P. Raffaelle, S.M. Hubbard, Open-circuit voltage improvement of inas-gaas quantum-dot solar cells using reduced inas coverage, IEEE J. Photovolt. 2 (3) (2012) 269–275.

[10] A. Martí, N. López, E. Antolin, E. Cánovas, C. Stanley, C. Farmer, L. Cuadra, A. Luque, Novel semiconductor solar cell structures: the quantum dot inter-mediate band solar cell, Thin Solid Films 511 (2006) 638–644.

[11] Y. Okada, T. Morioka, K. Yoshida, R. Oshima, Y. Shoji, T. Inoue, T. Kita, Increase in photocurrent by optical transitions via intermediate quantum states in di-rect-doped inas/ganas strain-compensated quantum dot solar cell, J. Appl. Phys. 109 (2) (2011) 024301, http://dx.doi.org/10.1063/1.3533423.

[12] S. Polly, D. Forbes, K. Driscoll, S. Hellstrom, S. Hubbard, Delta-doping effects on quantum-dot solar cells, IEEE J. Photovolt. 4 (4) (2014) 1079–10857, http://dx.doi.org/10.1109/JPHOTOV.2014.2316677.

[13] P. Lam, S. Hatch, J. Wu, M. Tang, V.G. Dorogan, Y.I. Mazur, G.J. Salamo, I. Ramiro, A. Seeds, H. Liu, Voltage recovery in charged inas/gaas quantum dot solar cells, Nano Energy 6 (2014) 159–166, http://dx.doi.org/10.1016/j.nanoen.2014.03.016.

[14] T. Sogabe, Y. Shoji, M. Ohba, K. Yoshida, R. Tamaki, H.-F. Hong, C.-H. Wu, C.-T. Kuo, S. Tomić, Y. Okada, Intermediate-band dynamics of quantum dots solar cell in concentrator photovoltaic modules, Scientific reports 4.

[15] T. Kita, R. Hasagawa, T. Inoue, Suppression of nonradiative recombination process in directly si-doped inas/gaas quantum dots, J. Appl. Phys. 110 (10) (2011) 103511.

[16] X. Yang, K. Wang, Y. Gu, H. Ni, X. Wang, T. Yang, Z. Wang, Improved efficiency of inas/gaas quantum dots solar cells by si-doping, Sol. Energy Mater. Sol. Cells 113 (2013) 144–147.

[17] K. Driscoll, M.F. Bennett, S.J. Polly, D.V. Forbes, S.M. Hubbard, Effect of quantum dot position and background doping on the performance of quantum dot enhanced gaas solar cells, Appl. Phys. Lett. 104 (2) (2014) 023119, http://dx.doi.org/10.1063/1.4862028.

[18] A. Markus, J. Chen, O. Gauthier-Lafaye, J. Provost, C. Paranthoen, A. Fiore, Im-pact of intraband relaxation on the performance of a quantum-dot laser, IEEE J. Quantum Electron. 9 (5) (2003) 1308–1314.

[19] P.S. Zory, Quantum Well Lasers, Academic Press, United States of America, 1993.

[20] A.C.M. Gioannini, F. Cappelluti, Impact of carrier dynamics on the photovoltaic performance of quantum dot solar cells, IET OptoelectronicsAccepted for publication.

[21] T. Morioka, Y. Okada, Dark current characteristics of inas/ganas strain-com-pensated quantum dot solar cells, Phys. E: Low. -Dimens. Syst. Nanostruct. 44 (2) (2011) 390–393.

[22] H.J. Hovel, Semiconductors and semimetals. Solar cells, Academic Press, Inc., New York, Vol. 11, 1975.

[23] P. Würfel, U. Würfel, Physics of Solar Cells: From Basic Principles to Advanced Concepts, John Wiley & Sons, United States, 2009.

[24] V. Mitin, V. Pipa, A. Sergeev, M. Dutta, M. Stroscio, High-gain quantum-dot infrared photodetector, Infrared Phys. Technol. 42 (3) (2001) 467–472.

[25] F.K. Tutu, P. Lam, J. Wu, N. Miyashita, Y. Okada, K.-H. Lee, N.J. Ekins-Daukes, J. Wilson, H. Liu, Inas/gaas quantum dot solar cell with an alas cap layer, Appl. Phys. Lett. 102 (16) (2013) 163907, http://dx.doi.org/10.1063/1.4803459.

[26] K. Sablon, J. Little, N. Vagidov, Y. Li, V. Mitin, A. Sergeev, Conversion of above-and below-bandgap photons via inas quantum dot media embedded into gaas solar cell, Appl. Phys. Lett. 104 (25) (2014) 253904.

[27] Y.D. Jang, J. Park, D. Lee, D.J. Mowbray, M.S. Skolnick, H.Y. Liu, M. Hopkinson, R.A. Hogg, Enhanced room-temperature quantum-dot effects in modulation-doped inas/gaas quantum dots, Appl. Phys. Lett. 95 (17) (2009) 171902.

[28] E.C. Le Ru, J. Fack, R. Murray, Temperature and excitation density dependence of the photoluminescence from annealed inas/gaas quantum dots, Phys. Rev. B 67 (2003) 245318.

[29] S. Sanguinetti, D. Colombo, M. Guzzi, E. Grilli, M. Gurioli, L. Seravalli, P. Frigeri, S. Franchi, Carrier thermodynamics in InAs $sin_x ga_{1-x}$As quantum dots, Phys. Rev. B 74 (2006) 205302.